Journal of
Synchrotron
Radiation

ISSN 0909-0495

Received 16 June 2006
Accepted 23 August 2006

Three-dimensional visualization of the inner structure of single crystals by step-scanning white X-ray section topography

Taihei Mukaide,[a]* Kentaro Kajiwara,[b] Takashi Noma[a] and Kazuhiro Takada[a]

[a]Canon Research Center, CANON Inc., Japan, and [b]Japan Synchrotron Radiation Research Institute, Japan. E-mail: mukaide.taihei@canon.co.jp

Visualization of the three-dimensional distribution of the crystal defects of large single crystals of calcium fluoride has been demonstrated by white X-ray section topography using sheet-like X-rays (BL28B2 at SPring-8). An image of the three-dimensional distribution of the crystal defects was reconstructed by stacking section topographs, which expressed the images of cross sections of the sample. The section topographs were recorded using a CMOS flat-panel imager or a CCD detector combined with scintillator (Gd_2O_2S:Tb) and relay lens system. The section topographs were measured by repeating cycles of exposure and sample translation along the direction perpendicular to the top face of the sample. Using high-brilliance and high-energy white X-rays ($\sim$60 keV) efficiently, visualization of the three-dimensional structure of subgrains of a sample of up to 60 mm in diameter was achieved. Furthermore, the three-dimensional distribution of the glide plane in the crystal was visualized by reconstructing the linear contrast of the glide plane.

© 2006 International Union of Crystallography
Printed in Great Britain – all rights reserved

Keywords: white X-ray topography; three-dimensional reconstruction; calcium fluoride; glide system.

1. Introduction

Single-crystal materials are used for key components in a wide range of fields from electronic devices to optics. The quantity and distribution of crystal defects are important for applications, and are related to properties such as electron mobility and refractive index.

X-ray topography is a powerful technique for analyzing the crystal defects of single crystals (Lang, 1958*a*,*b*). However, in-house X-ray topography equipment cannot detect the deep parts within bulky single crystals non-destructively because of absorption of incident and reflected X-rays.

In the case of single-crystalline materials for optics, it is important to understand the relationship between crystal defects and optical properties. Data concerning crystal defects deep within the crystal as well as at the surface are very important because the inhomogeneity of optical properties such as refractive index or birefringence emerges as an integrated value along the optical axis.

For instance, a single crystal of calcium fluoride (CaF_2) is an attractive material for ultraviolet optics because of its high transparency to ultraviolet light and optical isotropy (Rothschild *et al.*, 1996; Bloomstein *et al.*, 1997). However, when using such material for the lenses of a deep UV optical lithography system, even extremely small inhomogeneity of optical properties could cause serious problems for the performance of image formation. However, it is extremely difficult to detect the inhomogeneity of optical properties of a thin sample. Therefore, a technique for visualizing crystal defects deep within large single crystals is needed.

Large single crystals of CaF_2 are generally grown by the Bridgman–Stockbarger method (Molchanova *et al.*, 2005; Senguttuvan *et al.*, 2005). As the size of the crystal increases, it becomes more difficult to control crystal defects. In particular, the occurrence of grain boundaries during the crystal growth process is a serious problem hindering the growth of large crystals along selective orientation. Therefore, three-dimensional imaging of the distribution of crystal defects is valuable for improving the crystal growth process as well as the furnace used for crystal growth, because the distribution of the crystal defects of the grown crystal contains information about the thermal history. Hence, to improve the homogeneity of optical properties, it is important to visualize the crystal defects deep within large single crystals.

Measurements of the distribution of crystal defects in bulky single crystals have been performed using monochromated high-energy and high-brilliance synchrotron radiation (Ludwig *et al.*, 2001). Three-dimensional images of crystal defects were reconstructed from a series of images that were recorded by tomographic acquisition (topo-tomography). This method was very effective for nearly perfect crystals. However, it is not suitable for measuring the distribution of

subgrains, which are surrounded by low-angle grain boundaries, of imperfect single crystals using monochromatic X-rays because the incident angle of X-rays under Bragg conditions are different for each subgrain. In other words, using monochromatic X-rays provides only partial information about the subgrains, and this method requires considerable effort to adjust the diffraction vector to the rotation axis.

On the other hand, high-energy and high-brilliance white X-rays are well suited for measuring the distribution of subgrains deep within bulky imperfect crystals since the Bragg conditions of all subgrains are satisfied. One of the advantages of using white X-rays is that the recorded intensity of diffracted X-rays is stronger than that recorded using monochromatic X-rays because the projection also contains high-order reflections, which is useful for measuring large crystals. Furthermore, white X-rays are suitable for understanding the properties of crystal defects since the X-rays diffracted by several planes can be detected simultaneously by using a large area detector such as an imaging plate or X-ray film.

In this study we demonstrate the measurement of the distribution of crystal defects within bulky single crystals of CaF_2 by step-scanning white X-ray section topography. We also visualize the three-dimensional distribution of the subgrains and crystal defects by reconstructing the section topographs.

2. Experimental

Experiments were performed at beamline BL28B2 of SPring-8. Details of the specifications of the beamline have been reported elsewhere (Chikaura *et al.*, 2001). A schematic illustration of the experimental set-up is shown in Fig. 1. The white X-rays from the bending magnet as source were shaped as a sheet-like beam of size between 10 mm and 30 mm (horizontal) × 0.1 mm (vertical) in accordance with the size of the samples by the slits. We generally used an absorber made of aluminium (7 mm thick) to avoid damaging the sample by the absorption of low-energy X-rays, as local heating by such absorption causes crystal defects. Furthermore, if the diffracted X-rays were too strong, an absorber made of Cu was used in combination with the Al absorber.

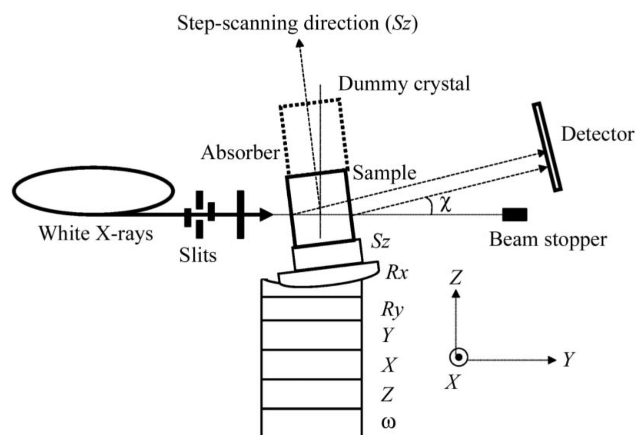

Figure 1
Schematic illustration of the experimental set-up. The goniometer is composed of several stages, *i.e.* Sz, Rx, Ry, Y, X, Z and ω. The dummy crystal was set on top of the sample. Diffracted X-rays were detected by the area detector. Measurements were carried out by repeatedly performing exposure and translation of the sample along the Sz and X axes.

A photograph of single crystals of CaF_2 is shown in Fig. 2. The samples were cut into cylinders of several sizes, between 30 mm and 60 mm in diameter and between 30 mm and 50 mm in thickness, from ingots of CaF_2, which were grown along the (1 1 1) orientation by the Bridgman–Stockbarger method under vacuum. The top faces of most samples were a (1 1 1) plane. The top and bottom faces of the sample were polished precisely. The sample was set on the goniometer composed of a Z-stage (Sz) which moved along the direction perpendicular to the top face of the sample, swivel stages (Rx, Ry) which rotated around the X or Y axis, XYZ stages and a rotation stage (ω). Section topographs of the samples were recorded using a CMOS flat-panel imager (C7942, Hamamatsu Photonics) (Yagi *et al.*, 2004) or a CCD detector (C4880-17, Hamamatsu Photonics) combined with scintillator (Gd_2O_2S:Tb) and 1:1 relay lens system (Suzuki *et al.*, 1999). The size of each pixel of these detectors was about 50 μm × 50 μm and 12.6 μm × 12.6 μm, respectively, and the size of each image of the detectors was 2240 pixels × 1872 pixels and 1000 pixels × 1018 pixels. Since the spatial resolution due to the angular divergence of incident X-rays is smaller than the pixel size, it is easy to improve the spatial resolution further by thinning the incident X-ray and changing the zoom ratio of the relay lens in the case of the CCD detector. However, we decided on the above set-up condition because it takes time to measure such a large sample. These detectors were attached on the stage of the χ axis and placed at an appropriate distance from the sample to avoid overlapping each Laue spot of interest. A dummy crystal, which had the same size but different orientation as the sample, was placed on the sample in order to make uniform the effect of absorption of the diffracted X-rays, which exit from the top face of the sample. To be more precise, all diffracted X-rays exited from the side of the dummy crystal or the sample.

First we adjusted the incident angle (Rx) of the X-rays and the distance between the detector and the sample by monitoring the intensities of the diffracted X-rays from the plane of

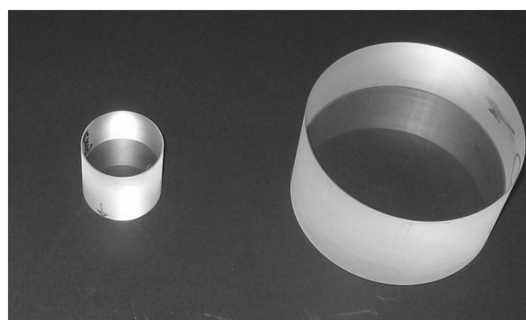

Figure 2
Photograph of the single crystals of CaF_2. Left: 30 mm diameter and 30 mm thickness. Right: 60 mm diameter and 50 mm thickness. All samples were grown by the Bridgman–Stockbarger method.

interest and the distortion of the image in the vertical direction of the detector. No other strict adjustments are needed. We then recorded data of all cross sections of the sample by repeating exposure and translation of the sample along the X axis and the Sz axis in accordance with the size of the samples. The exposure time of each image was between 1 s and 15 s depending on the intensity of the image, and the step size of translation along the Sz axis was 0.1 mm. The three-dimensional images were reconstructed by stacking the section topographs and analyzed by using commercially available visualization software (AMIRA, Version 3.1, TGS, San Diego, USA).

3. Results and discussion

Fig. 3 shows an example of the section topographs corresponding to the cross section of the sample, which was 30 mm in diameter, recorded by the CMOS flat-panel imager. The sample-to-detector distance was 740 mm. Even though the diameter of the sample was 30 mm, the images of several planes were detected at the same time with little overlapping using the CMOS flat-panel imager. It took about 30 min to measure all section topographs of this sample. It was clear that this sample was composed of many subgrains. The subgrain boundaries in the image were overlapping or separated from each other because of the differences in the incident angle for diffraction planes of each subgrain. Variations in intensity in the subgrains corresponded to crystal defects such as dislocations. The approximate value of the misorientation angle between subgrains around the X axis was obtained from the overlapping or separating width of subgrain boundaries of the image, the scattering vector of which lay in the YZ plane. The misorientation angle $\Delta\varphi$ is given by

$$\Delta\varphi = \frac{l\cos^2(2\theta_B - \chi)}{2L},$$

where l is the overlapping or separating width of a subgrain boundary, L is the sample-to-detector distance and $2\theta_B$ is the scattering angle (Milita *et al.*, 2001). From the section topograph shown in Fig. 3, the typical values of $\Delta\varphi$ are rather small ($\sim 10^{-2}$ deg).

The three-dimensional reconstruction was performed by simply stacking the section topographs. In the case of the topo-tomography method, deformation of the topographs by stress or strain is a serious problem in reconstruction. However, the reconstruction method in this study is less affected by such deformation. Fig. 4 shows three-dimensional images reconstructed from the section topographs of the {4 3 3} (*a*) and {1 1 1} (*b*) reflections. The scattering angle of each reflection was 15° by adjusting the crystal orientation. The image shown in Fig. 4(*a*) was expressed by three horizontal planes (top face, bottom face and intermediate plane), two vertical planes and a three-dimensional model of a subgrain, which is shown by the yellow surface. It was easy to recognize the network structure of subgrains within the crystal. The volume of this subgrain that was extracted from section topographs is about 270 mm^3. In this study we demonstrate the measurement of samples of up to 60 mm in diameter. Fig. 4(*b*) shows the three-dimensional reconstructed image of a part of this sample. The distance from the sample to the detector for the 60 mm-diameter sample was about 840 mm. By comparing these images, it is clear that the subgrains of the 60 mm-diameter sample were larger. Furthermore, the misorientation angle between the subgrains is relatively small since the overlapping or separation of the subgrain boundaries in the topographs was smaller than that of the sample of Fig. 4(*a*), even though the sample-to-detector distance was longer.

The integrated intensity of X-ray diffraction for each harmonic by a perfect single crystal is proportional to

$$I_{hkl} \propto \frac{|F_{hkl}|\,P(\lambda)\,\lambda^3}{\sin^2\theta_B}\exp(-\mu t/\cos\theta_B),$$

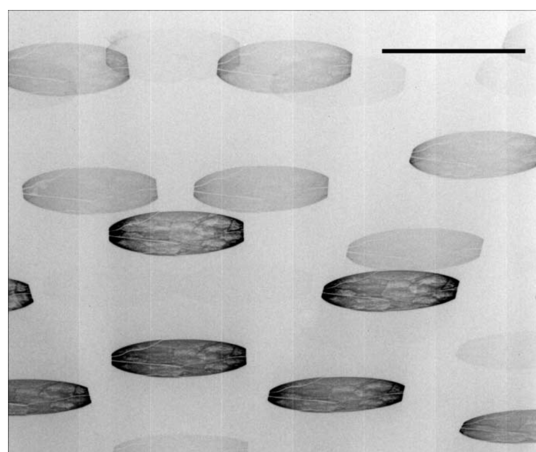

Figure 3
Typical Laue diffraction patterns of the sample. The scale bar is 30 mm. This image was detected by the flat-panel imager. The exposure time was 1 s. Several Laue diffraction patterns were recorded without overlapping. This sample was composed of many subgrains.

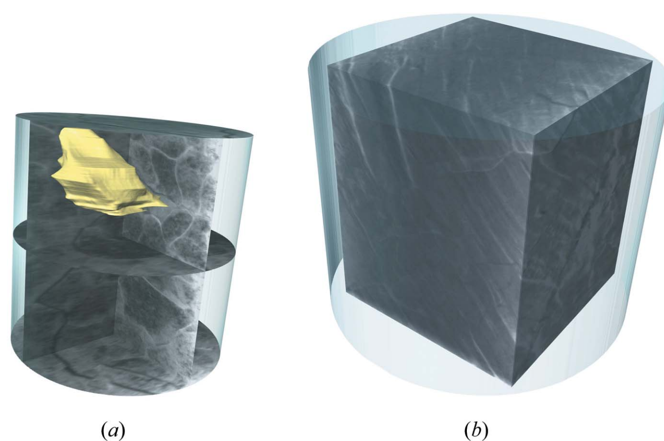

Figure 4
Three-dimensional reconstructed image of part of the sample from the section topographs. The image was reconstructed by using the section topographs of the (*a*) {4 3 3} and (*b*) {1 1 1} reflections. (*a*) 30 mm diameter and 30 mm thickness. This image indicates three horizontal planes, two vertical planes and the shape of a subgrain illustrated by the yellow surface. (*b*) 60 mm diameter and 50 mm thickness.

Table 1
Calculated integrated intensity I_{hkl} of each harmonic for diffracted X-rays from (1 1 1) to (10 10 10).

Calculation conditions were t = 30 mm and θ_B = 7.5°.

$h\ k\ l$	Energy (keV)	$P(\lambda)$	$\lvert F_{hkl} \rvert$	$\exp(-\mu t/\cos\theta_B)$	I_{hkl} (%)
1 1 1	15.056	1.174×10^{-6}	62.20	0.0000	0.00
2 2 2	30.112	0.333	6.81	0.0000	0.00
3 3 3	45.169	0.940	34.16	0.0005	1.97
4 4 4	60.225	0.965	45.85	0.0168	36.72
5 5 5	75.281	0.782	25.07	0.0610	30.17
6 6 6	90.337	0.578	9.60	0.1114	9.04
7 7 7	105.393	0.409	18.65	0.1558	10.92
8 8 8	120.450	0.280	25.90	0.1914	8.57
9 9 9	135.506	0.189	13.16	0.2198	2.37
10 10 10	150.562	0.125	2.49	0.2434	0.24

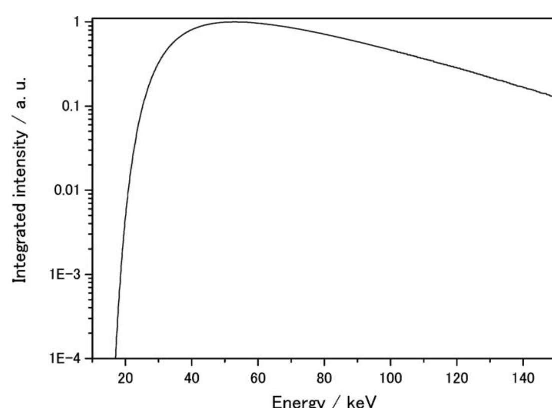

Figure 5
Calculated integrated intensity of the incident beam with Al absorber of thickness 7 mm at BL28B2. The low-energy component of the light source was removed by the absorber.

where $\lvert F_{hkl} \rvert$ is the structure factor, $P(\lambda)$ is the intensity of the incident X-rays with wavelength λ, θ_B is the Bragg angle, μ is the linear absorption coefficient and t is the thickness of the sample for the incident beam (Tuomi *et al.*, 1974; Hart, 1975). Fig. 5 shows the intensity of the incident beam with the absorber, which was calculated using the synchrotron radiation calculation code *SPECTRA* (Tanaka & Kitamura, 2001). The absorber cut the lower-energy X-rays (~20 keV) and protected the sample from local heating by absorption of such X-rays. The calculated integrated intensities for each harmonic of {1 1 1} in the case where t = 30 mm are shown in Table 1. The table shows that the diffracted X-rays from the (1 1 1), (2 2 2) and (3 3 3) planes were almost equal to zero due to the effects of the intensity of the incident beam and absorption. Therefore the contribution of high-energy X-rays ($\geq$60 keV) in the recorded image is very large under this size condition.

Fig. 6 shows a section topograph of {5 5 1} reflections from part of the sample, which was recorded by a CCD detector combined with scintillator and relay lens system. The top face of the sample had a 20° off-angle (1 1 1) towards the $\langle \bar{1}\ \bar{1}\ 2 \rangle$ direction. The size of the sample was 30 mm in diameter and 30 mm in thickness. The scattering vector was set on the YZ plane adjusting the crystal orientation.

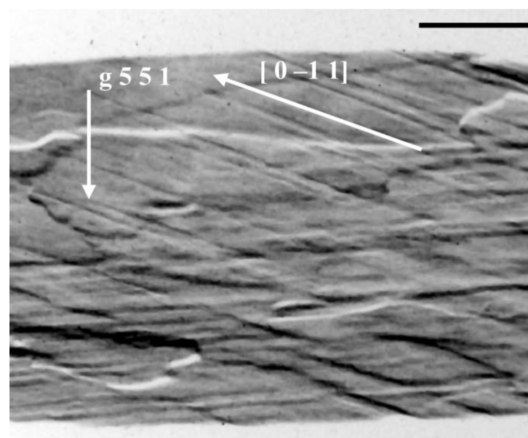

Figure 6
Section topograph of part of the sample detected by a CCD detector combined with scintillator and relay lens system. The scale bar is 2 mm. The subgrains and geometric linear texture are visible in this image.

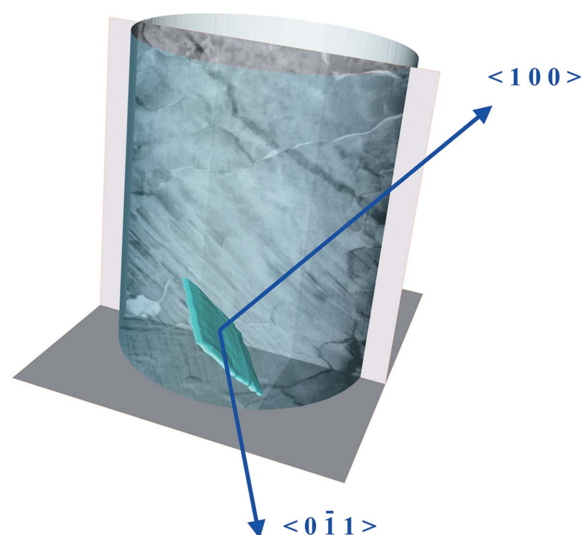

Figure 7
Three-dimensional reconstructed image of the sample. This image is composed of a horizontal plane, a vertical plane and the extracted plane of linear contrast of section topographs.

A geometric linear texture of the image appeared in the [0 $\bar{1}$ 1] direction. To obtain details of the contrast, a three-dimensional image was reconstructed by stacking section topographs. The reconstructed image of the sample is shown in Fig. 7. This image indicates a horizontal plane, a vertical plane and an extracted linear texture image from section topographs, which is expressed by the blue surface. There are linear textures at the lower part of the sample. The plane composed of linear contrast in the section topographs corresponds to the (0 0 1) plane by considering the direction and the tilt angle of the plane. In other words, this texture is indicated as the glide plane of the primary glide system {0 0 1} ⟨1 1 0⟩ of CaF_2. Such linear texture of crystal defects is detected by a direct image. From Table 1, the value of μt under a substantial range of energies is between about 1.6 and 4 in the case where t = 30 mm. Generally, the value of μt is less than 1 to obtain direct images. In the case of our samples, the size of the sample was

large but only the interior of the individual subgrains contributes to the dynamical diffraction because the energies of the diffracted X-rays from individual subgrains were different. Therefore, the substantial values of μt for most subgrains are less than 1 since the path length of incident X-rays within a subgrain of our sample is less than about 10 mm from Fig. 3 or Fig. 6. Since the image formation depends on the diffraction condition, further experiments for the defect characterization are now underway.

4. Conclusion

We have successfully visualized the three-dimensional distribution of the subgrains and glide plane of a CaF_2 single crystal by step-scanning white X-ray section topography. High-brilliance and high-energy white X-rays of synchrotron radiation made it possible to record the topographs of the large-size crystal in a short time. In this study we demonstrated the measurement of a sample which was up to 60 mm in diameter and 50 mm in thickness. The measurement results showed that the samples were composed of many subgrains and glide planes in some cases. The step-scanning white X-ray section topography is a very useful and simple technique for analyzing the three-dimensional distribution of crystal defects within large single crystals.

The synchrotron radiation experiments were performed at the BL28B2 at SPring-8 with the approval of the Japan Synchrotron Radiation Research Institute (JASRI) (proposal Nos. 2003B0663-NI-np-TU, 2004A0535-NI-np, 2004B0191-NI-np).

References

Bloomstein, T. M., Horn, M. W., Rothschild, M., Kunz, R. R., Palmacci, S. T. & Goodman, R. B. (1997). *J. Vac. Sci. Technol. B*, **15**, 2112–2116.

Chikaura, Y., Iida, S., Kawado, S., Mizuno, K., Kimura, S., Matsui, J., Umeno, M., Ozaki, T., Shimura, T., Suzuki, Y., Izumi, K., Kawasaki, K., Kajiwara, K. & Ishikawa, T. (2001). *J. Phys. D*, **34**, A158–162.

Hart, M. (1975). *J. Appl. Cryst.* **8**, 436–444.

Lang, A. R. (1959*a*). *Acta Cryst.* **12**, 249–1755.

Lang, A. R. (1959*b*). *J. Appl. Phys.* **30**, 1748–1755.

Ludwig, W., Cloetens, P., Härtwig, J., Baruchel, J., Hamelin, B. & Bastie, P. (2001). *J. Appl. Cryst.* **34**, 602–607.

Milita, S., Maccagnani, P., Angelucci, R. & Servidori, M. (2001). *J. Electrochem. Soc.* **148**, G439–G446.

Molchanova, A., Friedricha, J., Wehrhanc, G. & Müller, G. (2005). *J. Cryst. Growth*, **275**, 629–637.

Rothschild, M., Burns, J. A., Cann, S. G., Forte, A. R., Keast, C. L., Kunz, R. R., Palmateer, S. C., Sedlacek, J. H. C., Uttaro, R., Grenville, A. & Corliss, D. (1996). *J. Vac. Sci. Technol. B*, **14**, 4157–4161.

Senguttuvan, N., Aoshima, M., Sumiya, K. & Ishibashi, H. (2005). *J. Cryst. Growth*, **280**, 462–466.

Suzuki, Y., Yagi, N., Umetani, K., Kohmura, Y. & Yamasaki, K. (1999). *Proc. SPIE*, **3770**, 13–22.

Tanaka, T. & Kitamura, H. (2001). *J. Synchrotron Rad.* **8**, 1221–1228.

Tuomi, T., Naukkarinen, K. & Rabe, P. (1974). *Phys. Status Solidi A*, **25**, 93–106.

Yagi, N., Yamamoto, M., Uesugi, K. & Inoue, K. (2004). *J. Synchrotron Rad.* **11**, 347–352.